https://doi.org/10.5194/egusphere-2026-2865
Preprint. Discussion started: 22 July 2026

Nocturnal tropospheric gravity waves in a double-jet duct over the southern Taklimakan Desert: lidar observations and WRF simulations

Sihan Liu[1,2], Tianwen Wei[1*], Ning Zhang[2], Fangzhi Wei[1], Xinyuan Liang[1], Qian Huang[1], Yuan Wang[3], Haiyun Xia[1]

[1]State Key Laboratory of Climate System Prediction and Risk Management (CPRM), School of Atmospheric Physics, Nanjing University of Information Science & Technology, Nanjing, 210044, China.
[2]Nanjing-Helsinki Institute in Atmospheric and Earth System Sciences, Nanjing University, Nanjing 210023, China
[3]College of Meteorology and Oceanography, National University of Defense Technology, Changsha 410073, China

Correspondence to: Tianwen Wei (twwei@nuist.edu.cn)

Abstract. Atmospheric gravity waves can transport momentum and energy and couple different atmospheric layers. Their propagation and dissipation have been widely studied in the stratosphere and mesosphere, whereas their excitation and trapping within tropospheric double-jet ducts remain less well constrained. Here we combine coherent Doppler wind lidar (CDWL) observations at Minfeng, ERA5 reanalysis, and WRF simulations to investigate how a nocturnal double-jet structure over the southern Taklimakan Desert excites and modulates tropospheric gravity waves. Three events in September 2021 occurred under a similar configuration, with a lower-level easterly jet below 4 km, an upper-level westerly jet at 6-7 km, and a weak-wind layer between them. Oscillations of 10-20 min occurred within the weak-wind layer, with maximum amplitudes near the strong shear zone at the base of the westerly jet, suggesting a role for shear-related dynamical instability in wave generation. ERA5 buoyancy-frequency profiles show a stable layer near 4-6 km that favored thermal ducting, and Scorer-parameter diagnostics further indicate concurrent Doppler ducting. As the easterly jet intensified, the waveguide compressed and wave frequencies increased, consistent with a shift of trapped modes toward higher frequencies. WRF reproduced the first two cases reasonably well, yielding dominant horizontal wavelengths of 7-14 km and eastward phase speeds near 6 m s^{-1}, but showed substantial discrepancies in the third. These results indicate that nocturnal double-jet structures can act as an effective tropospheric waveguide by trapping gravity waves through thermal and Doppler ducting and shifting trapped modes toward higher frequencies as the duct evolves.

https://doi.org/10.5194/egusphere-2026-2865
Preprint. Discussion started: 22 July 2026

1. Introduction

Gravity waves are oscillations supported by buoyancy in a stably stratified atmosphere and are generated by a wide range of processes, including topographic forcing, convection, wind shear, jet streams, frontal systems, and ageostrophic adjustment (Xue et al., 2020; Ma & Qin, 2025; Ding et al., 2025; Fritts & Nastrom, 1992; Plougonven & Zhang, 2014; Knoop et al., 2026). They play an important role in atmospheric dynamics across a broad range of scales (Nappo, 2013). On large scales, gravity waves transport momentum and energy upward and influence the circulation and thermal structure of the middle and upper atmosphere (Holton, 1983; Vincent & Joan Alexander, 2000; Sato & Hirano, 2019). On mesoscales, research concentrates on the interactions between gravity waves and convective systems(Hoffmann & Alexander, 2010; Ma & Qin, 2025), mountain waves generated by topographic forcing and their associated downslope winds and clear-air turbulence (Alexander & Grimsdell, 2013; Durran, 1990; Lott, 2016; Plougonven & Zhang, 2016). On smaller scales, research has increasingly emphasized the interaction between gravity waves and boundary-layer turbulence (J. Sun et al., 2015; Zaitseva et al., 2022).

Gravity waves do not always propagate freely in the vertical. Under suitable stratification and wind conditions, their energy can be trapped within a limited altitude range, leading to ducted propagation. Atmospheric ducting suppresses vertical leakage of wave energy while enhancing horizontal propagation distance (Nappo, 2013; Nyassor et al., 2025). Two primary ducting mechanisms exist: thermal ducting, formed by vertical variations in temperature stratification (e.g.inversions), and Doppler ducting, induced by vertical wind shear (Dong et al., 2021; Knoop et al., 2026). Jet streams, as strong wind shear zones in the troposphere, provide ideal conditions for the formation of Doppler ducts (Chimonas & Hines, 1986). In particular, double jet structures, with their unique wind profiles, may provide especially suitable conditions for wave trapping and modal selection. However, their role in modulating tropospheric gravity waves remains insufficiently understood.

Previous observational and modeling studies have focused predominantly on gravity waves in the stratosphere and mesosphere, where wave amplitudes are generally larger and easier to detect (Fritts & Alexander, 2003). Satellite remote sensing, radiosondes, aircraft measurements, radar and lidar have enabled systematic characterization of wave properties in the stratosphere and mesosphere (Baumgarten et al., 2015; Dong et al., 2021; Dou et al., 2014; Gorbunov & Kan, 2024; Murphy et al., 2014; Stober et al., 2018; Toms et al., 2017). High-resolution numerical models have likewise been widely used to investigate gravity-wave generation, propagation, dissipation, and drag effects on the large-scale circulation (Alexander & Holton, 1997; Dong et al., 2021; Miyoshi et al., 2014). By contrast, tropospheric gravity waves remain less well characterized, even though the troposphere is the primary source region of atmospheric gravity waves (Plougonven & Zhang, 2014). This observational gap is particularly important for ducted gravity waves, whose trapped propagation may influence boundary-layer perturbations, turbulence generation, local land-atmosphere exchange, and aviation safety (Bramberger et al., 2017; Zaitseva et al., 2022; Zhang et al., 2022).

For studies of tropospheric gravity waves, CDWL provides a valuable observational tool because of its high temporal and vertical resolution and its ability to continuously resolve wave fine structure and evolution (Chouza et al., 2016; Gisinger et al., 2020; Jia et al., 2019; Shangguan et al., 2022; Witschas et al., 2017). However, single-point lidar observations inherently lack horizontal spatial information, limiting direct determination of horizontal wavelengths and propagation directions. High-resolution numerical simulations are therefore needed to complement the observations by providing three-

https://doi.org/10.5194/egusphere-2026-2865
Preprint. Discussion started: 22 July 2026

dimensional wave structure, source diagnostics, and the dynamical and thermodynamical background conditions relevant to ducting. Mesoscale models such as the Weather Research and Forecasting (WRF) model have been widely used for this purpose and can explicitly resolve kilometer-scale gravity waves (Costantino et al., 2015).

The southern margin of the Taklimakan Desert provides a favorable environment for such a study. The complex topography of the Tibetan Plateau and surrounding mountain ranges strongly modulates the regional wind field and atmospheric stratification through both thermal and mechanical forcing. Nocturnal low-level jets occur frequently with an annual frequency exceeding 60% over the Taklimakan Desert, with dominant easterly or east-northeasterly flow (J. M. Ge et al., 2016; Wang et al., 2026). In summer, the westerly flow is further modified by the Tibetan Plateau and bifurcates near the Pamir Plateau, with the northern branch entering the Tarim Basin through the gap between the Tian Shan and the Kunlun Mountains (Zu et al., 2008). These regional conditions favor the development of layered jet structures and potentially provide a suitable environment for ducted gravity-wave propagation.

In this study, we investigate three nocturnal ducted tropospheric gravity-wave events observed in September 2021 by continuous CDWL measurements at Minfeng, located on the southern margin of the Taklimakan Desert. The observations are combined with ERA5 reanalysis and WRF simulations to examine the wave characteristics, the thermal and Doppler ducting environment, and the role of the double-jet structure in wave trapping and evolution. The paper is organized as follows. Section 2 describes the observation site, instrumentation, datasets, and WRF model configuration. Section 3 presents the observed wave characteristics, examines the ducting mechanisms, and compares the results with WRF simulations. Section 4 summarizes the main conclusions.

2. Observation and datasets

2.1 Observation site

The Taklimakan Desert, ranking as the world's second-largest shifting sand desert and China's most extensive desert region (Rittner et al., 2016; W. Sun & Gao, 2022). The observation site at Minfeng (37.06°N, 82.69°E; 1418 m above sea level), illustrated in Figure 1, is situated along the southern margin of the Taklimakan Desert, adjacent to the northern foothills of the Kunlun Mountains, and experiences pronounced Tibetan Plateau influences. This region is characterized by extended sunshine duration, intense solar radiation, minimal precipitation, and the convergence of eastward and westward airflows, rendering it one of China's most sand-storm-prone areas (J. Ge et al., 2008; Ming et al., 2019; Xing et al., 2024).

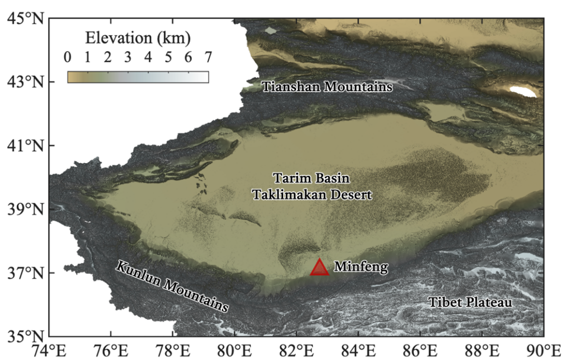

https://doi.org/10.5194/egusphere-2026-2865
Preprint. Discussion started: 22 July 2026

Figure 1. Digital Elevation Model (DEM) map of the Taklimakan Desert. The red triangle indicates the research site at Minfeng.

2.2 Coherent Doppler wind lidar

This investigation utilizes a compact CDWL operating in velocity azimuth display (VAD) scanning mode with an elevation angle of 70° (Elshora et al., 2024; Su et al., 2024). The system employs an eye-safe 1.5 μm wavelength and achieves temporal and radial resolutions of 1 s and 30 m, respectively. The lidar emits pulses at 10 kHz repetition frequency with 130 μJ pulse energy to achieve a maximum detection range of up to 15 km. The key operating parameters of the Doppler lidar system are summarized in Table 1. Detailed information about the validation and application of the lidar system can be found in our previous works (Jia et al., 2019; Wei et al., 2020, 2021; Su et al., 2024; Shangguan et al., 2017). In this study, the carrier-to-noise ratio (CNR), horizontal wind speed, wind direction, and vertical wind speed with 1 min temporal resolution were used.

Table 1. Key operating parameters of the Doppler lidar system

Parameter	Value
Wavelength (μm)	1.5
Pulse energy (μJ)	130
Repetition rate (kHz)	10
Diameter of telescope (mm)	100
Range gate length (m)	30
Sampling frequency (MHz)	500
Radial time resolution (s)	1
Scanning mode	VAD
Elevation angle (°)	70
Azimuth angle (°)	0-360

2.3 Radiosonde

Routine radiosonde observations used in this study were obtained from the Minfeng upper-air station (station ID 51839) in the China Meteorological Administration (CMA) observing network. Operational radiosonde stations in China widely used GTS1 digital radiosondes as key components of the L-band sounding system, which combines a digital radiosonde with a secondary wind-finding radar and provides vertical profiles of air temperature, pressure, relative humidity, wind speed, and wind direction from the surface to the middle stratosphere. In this study, the routine soundings at 08:00 and 20:00 Beijing Time (BJT) were used to evaluate the local thermodynamic structure and to assess the representativeness of the ERA5 profiles over Minfeng.

2.4 ERA5 reanalysis data

Hourly ERA5 reanalysis data produced by the European Centre for Medium-Range Weather Forecasts (ECMWF) were used to characterize the large-scale meteorological background. The pressure-level product, with a horizontal resolution of 0.25° × 0.25° and 37 pressure levels, was employed to describe the three-dimensional wind field over the Taklimakan Desert and surrounding regions. In addition, surface variables, including temperature, pressure, and near-surface winds, were used to examine the linkage between synoptic-scale forcing and local atmospheric processes near Minfeng.

At the Minfeng site, ERA5 vertical profiles of temperature and horizontal wind were extracted to diagnose the local thermodynamic and dynamical environments relevant to gravity-wave propagation

https://doi.org/10.5194/egusphere-2026-2865
Preprint. Discussion started: 22 July 2026

and trapping. Potential temperature (θ), and Brunt-Väisälä frequency squared (N^2) were further derived from the ERA5 pressure-level data and used to identify stable layers and possible thermal ducting structures.

2.5 WRF model description

The WRF model, version 4.7 (Weather Research and Forecasting model), reconstruct the three-dimensional physical structure of the observed gravity waves. A primary objective is to resolve the horizontal wave characteristics, including horizontal wavelength, wave orientation, and phase speed. Three nested domains were configured using a Lambert conformal projection, with horizontal resolutions of 4.5, 1.5, and 0.5 km for d01-d03, respectively. All domains employed 45 vertical eta levels with a model top at 50 hPa. The slope-radiation and terrain-shading options were enabled to account for topographic effects on radiation. For the physical parameterizations, the WRF Single-Moment 6-class (WSM6) microphysics scheme was used in all domains (Hong & Lim, 2006). The Kain-Fritsch cumulus parameterization was applied only in the outermost domain (Kain, 2004), while cumulus parameterization was turned off in the convection-permitting inner domains. Both longwave and shortwave radiation were represented using the Rapid Radiative Transfer Model for GCMs (RRTMG;Iacono et al., 2008). Turbulent mixing within the planetary boundary layer and near-surface exchange were treated using the Mellor-Yamada-Nakanishi-Niino (MYNN) Level 2.5 PBL scheme (Nakanishi & Niino, 2009; Olson et al., 2019) and the MYNN surface-layer scheme (Olson, 2021), respectively, coupled with the unified Noah land surface model (Chen & Dudhia, 2001; Tewari et al., 2004). The initial conditions and the lateral boundary conditions for the outermost domain were derived from the ERA5 reanalysis at 0.25° × 0.25° resolution.

3. Results and Discussion

3.1 Internal gravity waves (IGWs)

Ducted gravity waves can manifest as periodic oscillations in atmospheric pressure, horizontal and vertical wind speed, wind direction, temperature, and water vapor (Nappo, 2013). Figure 2 presents the time-height distributions of horizontal wind speed, wind direction, and vertical wind speed observed by the CDWL during three nocturnal periods. In all cases, the vertical structure is characterized by a lower-level easterly jet (~10 m s^{-1}) below 4 km, an overlying westerly jet (10-15 m s^{-1}) at 6-7 km, and a persistent weak-wind layer (< 2 m s^{-1}) sandwiched between them at 4-5 km. Within this weak-wind layer, pronounced high-frequency wave-like oscillations are clearly observed in vertical wind components. These fluctuations are closely collocated in time and altitude and extend from the base of the upper-level westerly jet into the weak-wind layer and fading out near the lower-level easterly jet.

Figure 3 shows the vertical profiles of horizontal wind speed, horizontal wind shear, and the maximum of vertical wind perturbation w' for the three cases. The horizontal wind speed and wind shear are averaged over a 30-minute window centered on the time of peak w' at each altitude level. The w' profile represents the maximum vertical wind perturbation at each level within the analysis time window (as defined in Eq. 1). In all three cases, the horizontal wind speed increases above 5 km, corresponding to the upper-level westerly jet. Furthermore, the altitude range of maximum w' (indicated by the grey shading) broadly coincides with the region of enhanced wind shear, suggesting that the observed gravity waves were likely generated by dynamical instability induced by the strong vertical wind shear of the upper-level westerly jet.

https://doi.org/10.5194/egusphere-2026-2865
Preprint. Discussion started: 22 July 2026

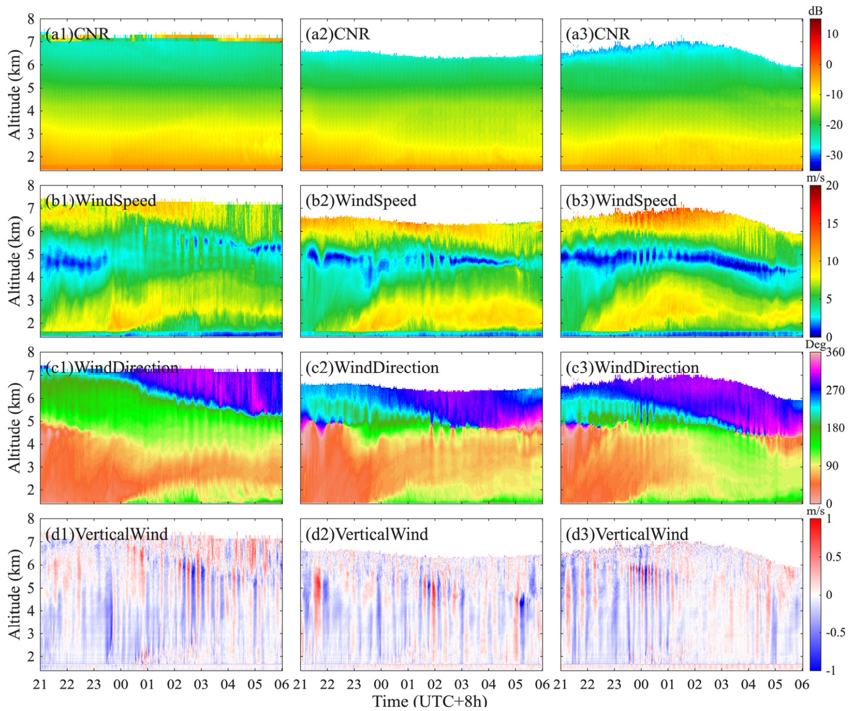

Figure 2. Time-height plot of (a1-a3) carrier-to-noise ratio (CNR), (b1-b3) horizontal wind speed, (c1-c3) horizontal wind direction, and (d1-d3) vertical wind speed observed by the Doppler wind lidar during three nocturnal periods: 21:00-06:00 BJT on 6-7 September, 7-8 September, and 17-18 September, 2021. All altitudes are given as above sea level (ASL).

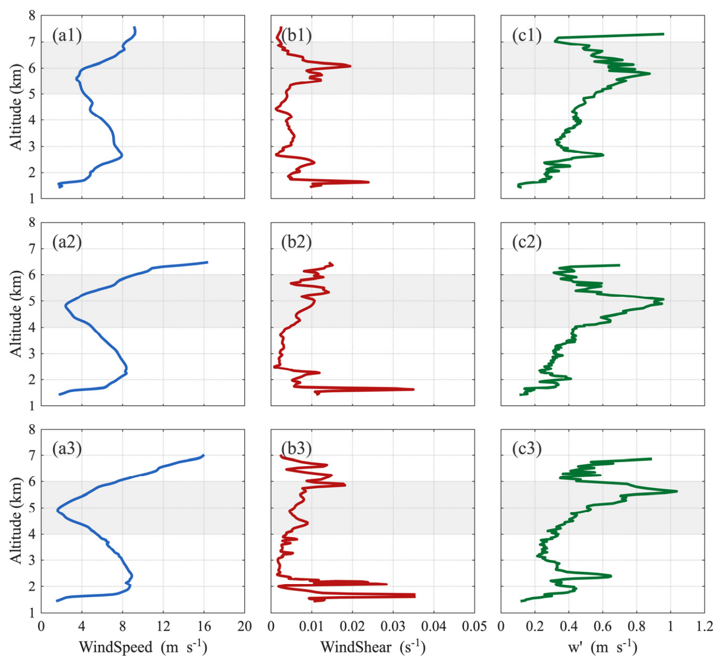

Figure 3. Vertical profiles of (a1-a3) horizontal wind speed, (b1-b3) horizontal wind shear, and (c1-c3) the maximum amplitude of vertical wind perturbation w'. These were observed on 02:00-04:00 7 September, 01:00-03:00 8 September, and 23:00 17 September -01:00 18 September 2021, respectively. Blue-shaded areas denote the regions of maximum w'.

To further characterize the wave activity in both the time and frequency domains, the continuous wavelet transform (CWT) was applied (Torrence & Compo, 1998). For each case, the horizontal and vertical wind components (*u, v, w*) measured by the CDWL were first resampled to 1-minute temporal resolution. Subsequently, wind data within the height range of the weak-wind layer were extracted and altitude-averaged to obtain representative time series. Figure 4 shows the wavelet power spectra overlaid with the corresponding height-averaged wind speed time series, highlighting the dominant oscillation periods and the time intervals of enhanced wave activity.

Overall, all three wind components exhibit pronounced and isolated wavelet power enhancement centers within the 10-30 min period band. These high-energy regions correspond closely to the wave-like oscillations seen in the wind time series. Specifically, for case 1 (Fig. 4a1-c1) and case 2 (Fig. 4a2-c2), the wavelet power spectrum of the vertical velocity exhibits a highly concentrated energy peak near 02:00 BJT at a period of approximately 20 min, indicating significant time-frequency localization. In case 3 (Fig. 4a3-c3), the wave activity appears earlier and is characterized by shorter periods of approximately 10-15 min, and the three-dimensional wind components exhibit clear time-frequency coherence. Additionally, for case 2 and case 3, the dominant period of the fluctuations is observed to shift progressively toward higher frequencies (shorter periods) with time. The coherent oscillation of horizontal and vertical wind components within the same frequency band is consistent with the polarization relations described by linear gravity wave theory, providing kinematic evidence for the wave nature of the observed disturbances (Fritts & Alexander, 2003).

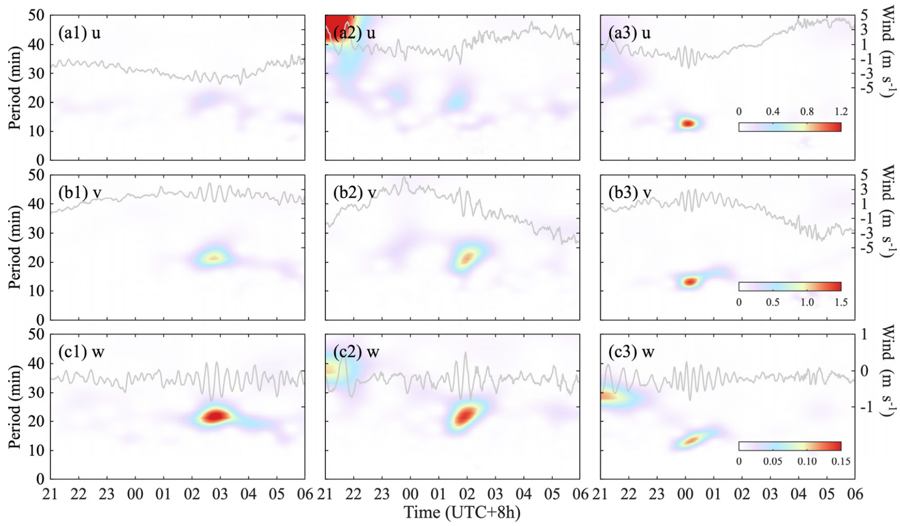

Figure 4. Continuous wavelet power spectra of wind speed within the weak-wind layer. Panels (a1-a3), (b1-b3), and (c1-c3) represent the wavelet power spectra of the height-averaged *u*, *v*, and *w* components for the three cases, respectively. The gray curves denote the corresponding height-averaged wind speed time series.

https://doi.org/10.5194/egusphere-2026-2865
Preprint. Discussion started: 22 July 2026

To further investigate the dynamical properties of the observed disturbances, perturbation wind fields were extracted and polarization relations were employed for analysis. A Reynolds decomposition was first applied to the height-averaged wind field to separate it into a slowly varying background component and a wave perturbation component:

$$q(t) = \bar{q}(t) + q'(t) \tag{1}$$

where $\bar{q}(t)$ denotes the background field, obtained using moving mean with time window of 60 min, and $q'(t)$ represents the residual perturbation.

Based on the linearized equations under the Boussinesq approximation, and assuming wave-like solutions of the form $\xi' = \tilde{\xi}(z) \cdot \exp[i(kx - \omega t)]$, the continuity equation yields the polarization relation (Nappo, 2013):

$$\tilde{u} = -\frac{m}{k} \cdot \tilde{w} \tag{2}$$

where k and m are the horizontal and vertical wavenumbers, respectively. When m is real, the wave propagates freely in the vertical direction, and the phase difference between w' and u' is theoretically 0° or 180°. In contrast, when m is purely imaginary, the phase difference is ±90°, and the wave becomes evanescent in the vertical direction, with its amplitude decaying exponentially away from the duct center. To quantify the phase relationship between the horizontal and vertical perturbations, A Hilbert transform was applied layer by layer to u' and w' series to obtain their instantaneous phases, from which the phase difference $\Delta\phi = \phi_u - \phi_w$ was computed at each level. To reduce artificial discontinuities caused by phase wrapping near ±180°, circular statistical averaging was employed for temporal averaging and 5-layer vertical smoothing (Mardia & Jupp, 2000), resulting in a continuous vertical profile of phase difference.

Figure 5 shows the altitude-averaged time series of u' and w' within the weak-wind layer. In all three cases, the two perturbation components exhibit coherent oscillations during the gray-shaded wave-active intervals, indicating organized wave motions in the layer. Their temporal relationship, however, differs between the earlier and later wave-active stages: the signals are clearly offset in the earlier stage, whereas their lead-lag relationship changes noticeably in the later stage after the intensification of the lower-level easterly jet. This evolution suggests a change in wave polarization characteristics. Figure 6 presents the vertical profiles of the phase difference between w' and u' for the three cases. In the initial stage (Fig. 6a), the phase difference is predominantly clustered around −90° throughout most of the observed altitude range, indicating that u' lags w' by approximately 90°. This is consistent with the theoretical prediction for a purely imaginary m, suggesting that the waves are vertically evanescent at this stage and that their energy cannot propagate freely in the vertical direction. In the later stage (Fig. 6b), following the intensification of the easterly jet, the phase difference shifts markedly relative to the initial stage. Within the 4-6 km layer, the phase differences in cases 1 and 2 cluster near 45°, whereas that in case 3 clusters near 135°, indicating that the wave behavior has evolved away from the initial evanescent state and toward a more vertically propagating mode in this altitude range. Below approximately 4 km, the wave perturbations diminish markedly, suggesting that the easterly jet may act as a reflecting layer that prevents downward energy propagation (Gill & Donn, 2016; Nappo, 2013). The physical mechanisms underlying this transition are discussed in Section 3.3.

https://doi.org/10.5194/egusphere-2026-2865
Preprint. Discussion started: 22 July 2026

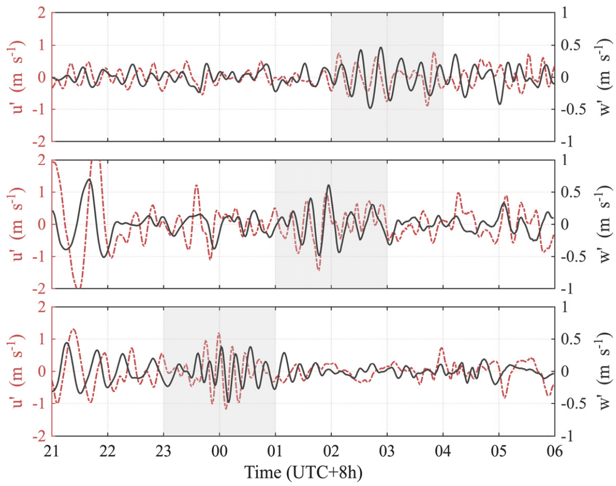

Figure 5. Time series of altitude-averaged u' (red dashed line, left axis) and w' (black solid line, right axis) perturbations within the weak-wind layer (4-5 km, ASL). Gray shaded regions denote the wave-active intervals selected for polarization analysis. Note the distinct lead-lag relationships between u' and w' in the earlier and later stages.

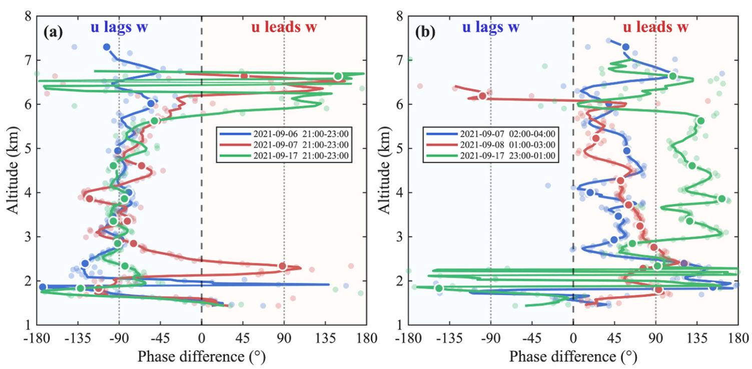

Figure 6. Vertical profiles of the phase difference between u' and w' for three cases. (a) Initial stage prior to the intensification of the easterly jet. (b) Stage after the intensification of the easterly jet. Dots indicate the raw phase-difference values at each altitude, and the colored solid lines denote the smoothed profiles derived from the Hilbert-transform-based analysis.

3.2 Ducting mechanism

3.2.1 Thermal duct

A thermal duct refers to an atmospheric layer of significantly enhanced static stability, typically bounded above and below by relatively weakly stable or near-neutral environments. The elevated N^2 within this layer implies a strong restoring force on vertically displaced air parcels, thereby inhibiting the vertical propagation of gravity waves. The static stability is quantified by N^2, defined as:

$$N^2 = \frac{g}{\theta}\frac{d\theta}{dz} \tag{3}$$

https://doi.org/10.5194/egusphere-2026-2865
Preprint. Discussion started: 22 July 2026

Figure 7 compares the vertical thermodynamic structure from radiosonde observations and ERA5 reanalysis for the three cases. In cases 1 and 2, both the radiosonde observations and ERA5 reanalysis consistently show a temperature inversion between 4 and 6 km altitude, accompanied by markedly elevated N^2 values in this layer, indicative of strong static stability. In contrast, case 3 exhibits a less distinct inversion structure, with comparatively weaker stratification than the preceding two cases. Although ERA5 shows some limitations in fully resolving the sharp temperature inversion, it successfully captures the dominant N^2 enhancement near 5 km associated with the steep vertical gradient of potential temperature, confirming its suitability for characterizing the ducting structures examined in this study. Figure 8 presents the spatio-temporal evolution of N^2 derived from ERA5 reanalysis data. All three cases exhibit a consistent vertical stratification structure: between 2 and 4 km, N^2 remains persistently low (~0.5×10^{-4} rad² s⁻²), corresponding to a weakly stable, near-neutral layer; above approximately 4 km, N^2 increases progressively, defining a strongly stable layer that acts as a thermodynamic waveguide, inhibiting the vertical propagation of wave energy and confining it to quasi-horizontal propagation. Notably, in case 3, the stable layer is comparatively weaker and situated at a somewhat higher altitude than in cases 1 and 2. This relatively weak and elevated stratification likely accounts for the deeper vertical extent of the wave oscillations observed at the initial time (21:00 BJT) in Figure 2, as the reduced trapping efficiency of the waveguide permits greater vertical penetration of wave energy.

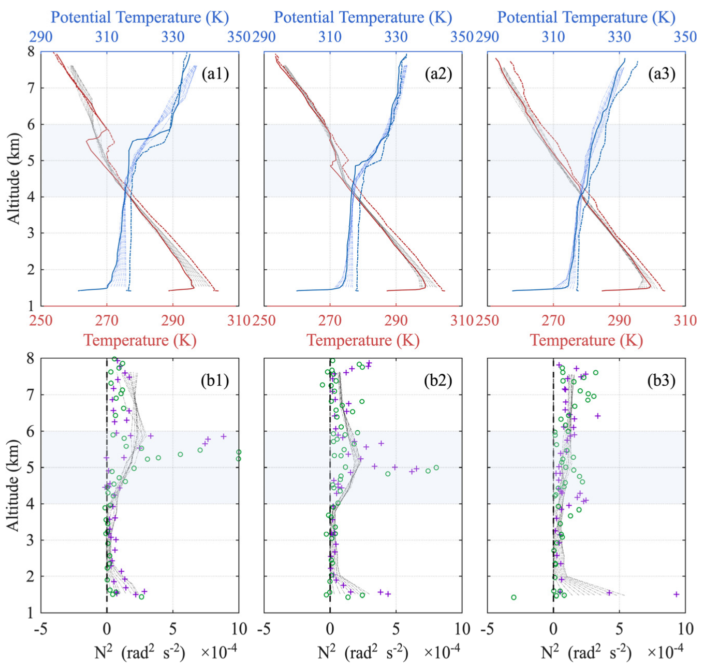

Figure 7. Vertical profiles of temperature, potential temperature, and Brunt-Väisälä frequency squared (N^2) from radiosonde observations and ERA5 reanalysis for the three cases. Panels (a1-a3) show temperature (lower horizontal axis, K) and potential temperature (upper horizontal axis, K). The red solid and dash-dotted lines denote radiosonde temperature at 08:00 and 20:00 BJT, respectively, and the blue lines the corresponding potential temperature; the gray dash-dotted lines show the hourly ERA5 profiles from 21:00 to 06:00 BJT. (b1-b3) Vertical profiles of the

https://doi.org/10.5194/egusphere-2026-2865
Preprint. Discussion started: 22 July 2026

Brunt-Väisälä frequency squared (N^2) with purple crosses and green open circles indicating radiosonde-derived values, and gray dash-dotted lines showing the hourly ERA5-derived profiles.

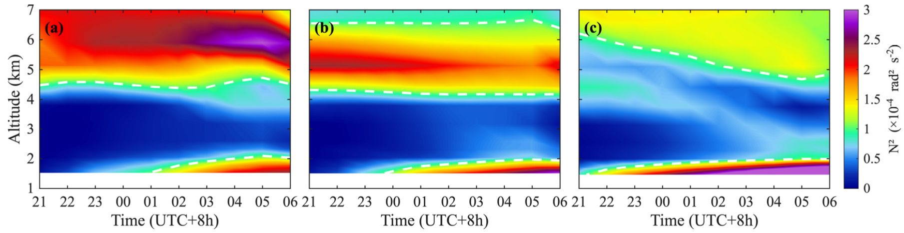

Figure 8. Time-height evolution of the squared buoyancy frequency (N^2) from ERA5 reanalysis for the three cases: (a) 6-7 September , 2021, (b) 7-8 September, 2021, and (c) 17-18 September, 2021. The white dashed contour marks the $N^2 = 1.0 \times 10^{-4}$ $rad^2\ s^{-2}$ isoline separating weakly and strongly stable layers.

3.2.2 Doppler duct

In addition to the trapping effect of the thermal stratification, the vertical shear of the background wind field is another critical factor governing the effective trapping of gravity waves. This wind-modulated wave-trapping mechanism is referred to as Doppler ducting (Fritts & Yuan, 1989). Figure 9 shows the horizontal wind fields on constant-altitude slices at 3, 4, 5, and 6 km for the three cases, superimposed on the DEM terrain background. Figure 10 presents the corresponding ERA5 surface fields, with panels (a1-a3) showing surface temperature and pressure and panels (b1-b3) showing the near-surface wind field.

During nighttime, the ERA5 near-surface fields show relatively higher pressure over the basin floor and lower pressure along the surrounding terrain (Fig. 10a1-a3). Together with the surface wind field, this pattern is consistent with pressure-gradient-driven divergent outflow from the basin interior. Concurrently, nocturnal radiative cooling along the northern slopes of the Kunlun Mountains favors the development of a downslope mountain-wind circulation (Elshora et al., 2025). These two airflows converge along the southern rim of the basin, establishing a lower-level easterly jet oriented parallel to the mountain ridge (Fig.10b1-b3). The upper-level westerly jet originates from the pronounced bifurcation of the westerly flow by the Tibetan Plateau (Yeh, 1950), placing the Minfeng station beneath the accelerating divergence zone of the northern branch jet (Fig. 9). At the interface between the easterly jet and westerly jet, a near-complete reversal of wind direction produces a transitional layer characterized by a wind speed minimum.

It should be noted that the observed gravity waves are unlikely to be classic lee waves generated by airflow over the mountain terrain. As shown in Figure 9, the westerly flow above 5 km is predominantly oriented parallel to the mountain ridge, with no significant cross-ridge component, which does not favor the dynamical conditions typically required for lee wave excitation. The observed gravity waves are therefore more plausibly attributed to the strong vertical wind shear associated with the dual-jet structure consisting of the easterly jet and the westerly jet, with a plausible wave source being the intense shear zone near the interface between the two jets, where dynamical instability is likely to develop.

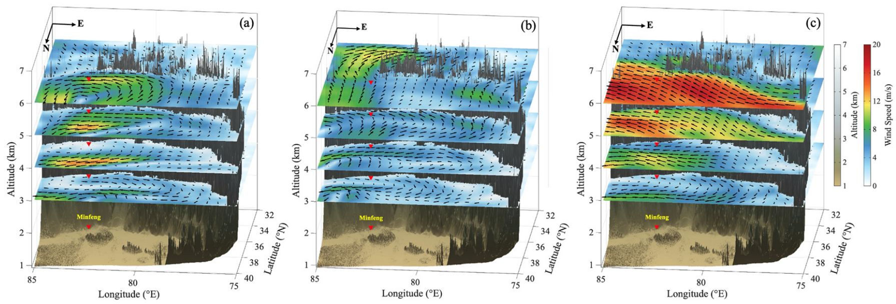

Figure 9. Horizontal wind slices over the Taklimakan Desert for the three cases derived from ERA5 reanalysis. The panels correspond to (a) 02:00 BJT, 7 September 2021; (b) 02:00 BJT, 8 September 2021; (c) 00:00 BJT, 18 September 2021. Horizontal wind speed (shaded; m s^{-1}) and wind vectors (black arrows) are shown on constant-altitude horizontal slices at 3, 4, 5, and 6 km, with the DEM shown as the underlying terrain. The red inverted triangle marks the location of Minfeng.

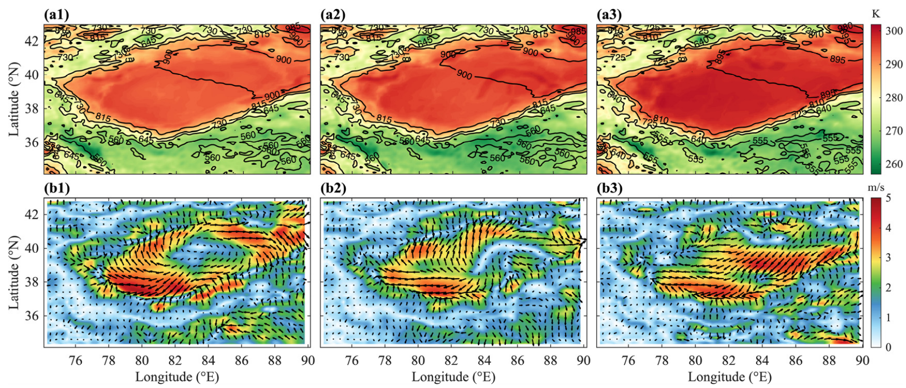

Figure 10. Surface meteorological fields for the three cases based on ERA5 reanalysis data. (a1-a3) Surface temperature (shaded, unit: K) and surface pressure (contours, unit: hPa); (b1-b3) horizontal wind speed (shaded, unit: m s^{-1}) and wind vectors at a height of 10 m. The columns correspond to the following times: (a1, b1) 02:00 BJT, 7 September 2021; (a2, b2) 02:00 BJT, 8 September 2021; (a3, b3) 00:00 BJT, 18 September 2021.

Following the clarification of the double-level jet's formation mechanism, it is essential to further elucidate the trapping and guiding effects of this dynamical structure on gravity wave propagation. To quantitatively assess the vertical propagation environment, the Scorer parameter (Q^2) from the Taylor-Goldstein equation is introduced:

$$Q^2 = \frac{N^2}{(c - u_0)^2} + \frac{u_0''}{c - u_0} - k^2 \quad (4)$$

where N is the buoyancy frequency, c is the horizontal phase speed, u_0 is the background wind speed, u_0'' is the second vertical derivative of the background wind, and k is the horizontal wavenumber.

Wave propagation is permitted within regions where $Q^2 > 0$, and when such a layer is bounded above and below by evanescent zones where $Q^2 < 0$, a classical Doppler duct is established. This ducting mechanism effectively traps gravity wave energy within the jet system, minimizing vertical leakage.

https://doi.org/10.5194/egusphere-2026-2865
Preprint. Discussion started: 22 July 2026

Meanwhile, as u_0 approaches c, the waves enter a critical layer region where their energy is absorbed by the background flow, thereby blocking further vertical penetration.

However, the single-lidar observations are insufficient to directly retrieve the horizontal wavenumber k and horizontal phase speed c, precluding a purely observation-based quantitative evaluation of the Q^2 profile. High-resolution WRF simulations are therefore employed to provide the three-dimensional wave structure alongside estimates of phase speed and horizontal wavenumber, enabling a more rigorous quantitative assessment of the ducting mechanisms.

3.3 WRF Simulation

The WRF-simulated background wind field at Minfeng was first compared with the lidar observations (Fig. 11). The model reproduces the observed layered flow configuration, including the lower-level northeasterly-to-easterly flow, the upper-level westerly jet, and the intervening weak-wind layer. However, the simulated lower-level flow is systematically located about 1 km lower than observed, which also shifts the weak-wind layer and the main wave-active region downward by roughly 1 km. This low bias may result from uncertainties in the representation of boundary-layer processes over complex terrain, smoothing of the background flow in the initial and boundary conditions, and the terrain-following vertical coordinate in WRF. Although it limits the exact altitude matching between simulations and observations, the model still captures the relative jet structure and shear configuration relevant to wave trapping. The simulation therefore provides a useful three-dimensional complement to the single-station lidar observations.

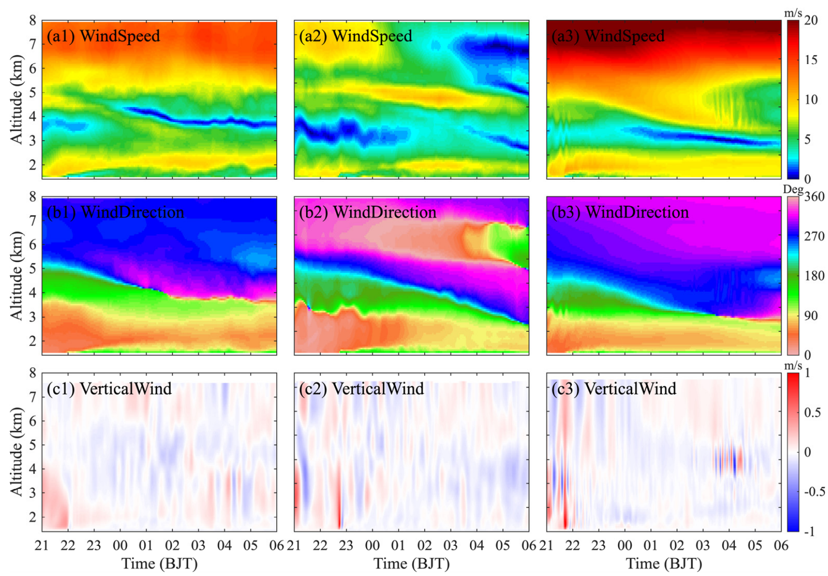

Figure 11. Time-height cross-sections of the WRF-simulated wind field at Minfeng for the three nocturnal cases. (a1-a3) horizontal wind speed, (b1-b3) horizontal wind direction, and (c1-c3) vertical wind speed during three nocturnal periods: 21:00-06:00 BJT on 6-7 September, 7-8 September, and 17-18 September, 2021.

Following the evaluation of the simulated background wind field, the three-dimensional wave structure can be examined more directly. Figure 12 presents longitude-altitude cross-sections of simulated vertical velocity along 37.06°N at selected times, illustrating the vertical structure and horizontal propagation

https://doi.org/10.5194/egusphere-2026-2865
Preprint. Discussion started: 22 July 2026

characteristics of the gravity waves. In all three cases, wave signals are mainly concentrated between 82°E and 83.5°E, close to the Minfeng site. On 7 September, the wave pattern is most pronounced, with clear alternating positive and negative vertical-velocity centers developing between about 3 and 5 km and becoming strongest at 02:40-03:00 BJT. On 8 September, a similarly coherent but more localized wave packet is evident, mainly confined to 3-4.5 km and characterized by a shorter horizontal scale. In contrast, the simulated wave signatures on 18 September are much weaker, with less distinct alternating structures and smaller amplitudes, indicating reduced organization of the wave field in that case. Consistent with the background-field comparison in Fig. 11, the simulated wave core is also located slightly lower than observed. It is also noted that the simulated wave signals in Fig. 12 are slightly spatially offset from the Minfeng site, which may partly account for the relatively weak vertical wind perturbations seen in Fig. 11c1-c3.

The horizontal wavelength characteristics of the simulated waves are further quantified by the FFT power spectra of WRF-simulated vertical velocity along the longitude direction at selected heights, as shown in Fig. 13. On 7 September, the dominant wavelength remains relatively stable at about 10-14 km. On 8 September, the dominant wavelength is shorter and more concentrated, clustering around 6-7 km. By contrast, on 18 September, the dominant spectral peak varies markedly among the selected times, ranging from about 8 to 17 km, and the overall spectral energy is weaker.

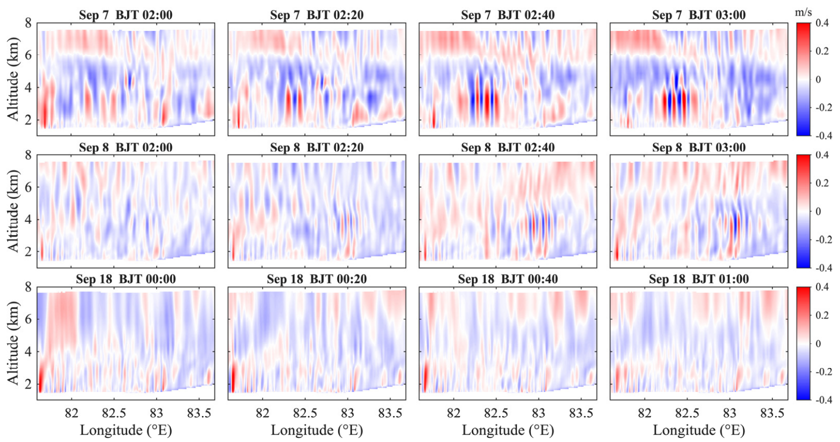

Figure 12. Longitude-altitude cross-sections of WRF-simulated vertical velocity (w) along 37.06°N at selected times. Columns show successive time snapshots, and rows correspond to 7 September (02:00-03:00 BJT), 8 September (02:00-03:00 BJT), and 18 September (00:00-01:00 BJT) 2021, respectively.

https://doi.org/10.5194/egusphere-2026-2865
Preprint. Discussion started: 22 July 2026

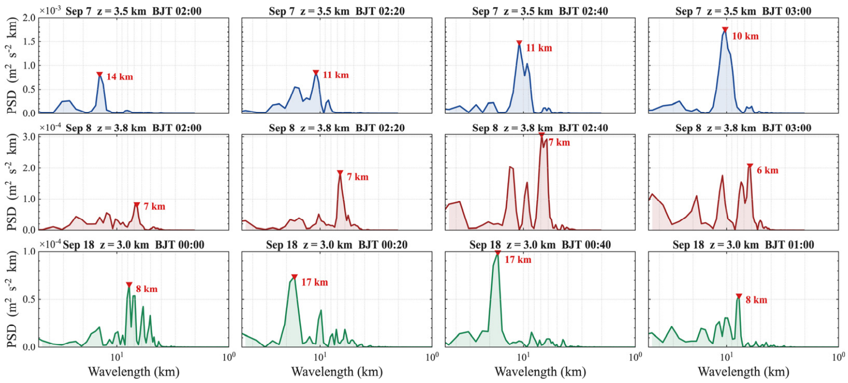

Figure 13. FFT power spectra of WRF-simulated vertical velocity along the longitude direction at selected heights. Columns correspond to the same time snapshots as in Figure 12, and rows correspond to September 7 (z = 3.5 km), September 8 (z = 3.8 km), and September 18 (z = 3.0 km), respectively. Red inverted triangles mark the dominant spectral peaks, and the corresponding dominant wavelengths (km) are labeled.

To characterize the horizontal propagation of the simulated gravity waves, Hovmöller diagrams of vertical velocity perturbation along 37.06°N were constructed for the three cases. In a Hovmöller diagram, longitude is plotted on the horizontal axis and time on the vertical axis, allowing the horizontal phase speed and propagation direction of the waves to be directly inferred from the inclination and slope of the streaks (Torrence & Compo, 1998). Figures 14(a-c) show the Hovmöller diagrams of vertical velocity along 37.06°N at selected altitudes for 7 September, 8 September, and 18 September, 2021, respectively. In all three cases, the waves propagate eastward. The horizontal phase speed is approximately 6.0 m s^{-1} on September 7 and September 8, and slightly lower at approximately 4.0 m s^{-1} on September 18.

To compare the simulations with the lidar observations, the dominant horizontal wavelength was estimated from spatial FFT analysis of the WRF-simulated vertical velocity fields, and the simulated wave period was then calculated as the ratio of wavelength to phase speed. The resulting parameters are summarized in Table 2. On 8 September, the simulated period (19 min) agrees well with the observed value (20 min), whereas on 7 September the simulated period (32 min) is somewhat longer than observed (20 min) but remains of the same order of magnitude. In contrast, the discrepancy is substantial on 18 September, when the simulated period (52 min) is much longer than the observed period (15 min). This mismatch likely reflects the limited ability of the model to reproduce the fine-scale structure and evolution of the wave field in that case.

Using the retrieved horizontal phase speeds, the Scorer parameter squared (Q^2) was further evaluated the diagnose the vertical propagation environment. Q^2 combines the effects of background wind and static stability and is commonly used to identify layers favorable for wave propagation and trapping. Regions with $Q^2 > 0$ are conducive to wave propagation, whereas regions with $Q^2 < 0$ correspond to evanescent layers in which wave amplitudes decay and partial reflection or trapping may occur. Figures 14(d-f) present the height-time cross-sections of Q^2 for the three cases. In all cases, a distinct sign-reversal from negative values below to positive values is evident near 5 km altitude. This indicates that wave activity is suppressed beneath this level, while within the overlying ducting layer the waves are sustained and propagate. The simulated Q^2 structure is also consistent with the phase-difference analysis shown in Fig. 6. During the initial stage, when the easterly jet and its associated evanescent layer were relatively weak,

https://doi.org/10.5194/egusphere-2026-2865
Preprint. Discussion started: 22 July 2026

the wave perturbations extended over a broader vertical range and exhibited comparatively larger amplitudes. As the easterly jet intensified, the evanescent layer deepened and its reflective effect became stronger, progressively confining the wave energy to a narrower altitude range.

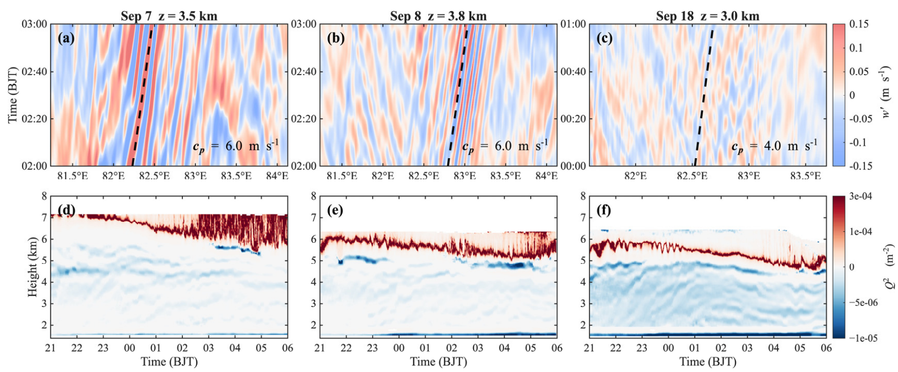

Figure 14. (a-c) Hovmöller diagrams of WRF-simulated vertical velocity perturbation (w') along 37.06°N for 7 September, 8 September, and 18 September, 2021, respectively. The black dashed line indicates the horizontal propagation of gravity waves, with its slope corresponding to the horizontal phase speed. (d-f) Height-time cross-sections of the Scorer parameter squared (Q^2) for the corresponding three cases. Red denotes regions with $Q^2 > 0$, favorable for wave ducting, whereas blue denotes regions with $Q^2 < 0$, corresponding to evanescent conditions.

Table 2. Wave parameters derived from WRF simulations and observations

	Sep 7	**Sep 8**	**Sep 18**
Simulated dominant wavelength (km)	11.5	6.8	12.5
Simulated phase speed (m s^{-1})	6	6	4
Simulated period (min)	32	19	52
Observed period (min)	20	20	15

In summary, the observed gravity wave activity appears to have been modulated by several interacting dynamical and thermodynamical processes. First, the intense vertical wind shear at the base of the westerly jet (WJ) likely provided a favorable environment for wave generation. Second, the shear interface at the lower boundary of the WJ, together with the underlying weak-wind layer, formed a Doppler duct, while the strongly stable layer associated with the temperature inversion acted as a thermal duct. The combined action of these two ducting mechanisms limited vertical energy leakage and favored the horizontal confinement of wave energy within a preferred altitude range. In addition, the lower-level easterly jet appears to have acted as a reflective barrier through the associated evanescent layer, whereas critical levels within the WJ may have absorbed part of the upward-propagating wave energy. Taken together, these processes suggest that the double-jet structure provided a dynamically favorable environment for the trapping and horizontal propagation of the nocturnal gravity waves observed in this study.

Beyond wave trapping and vertical confinement, an additional issue concerns the observed evolution of wave frequency. In the present cases, the strengthening of the easterly jet was accompanied by changes in the lower boundary and effective depth of the duct (Fig. 2), suggesting that the waveguide itself evolved during the event. According to ducting theory, a waveguide does not support a continuous spectrum of waves, instead, only discrete trapped modes satisfying specific vertical boundary conditions

https://doi.org/10.5194/egusphere-2026-2865
Preprint. Discussion started: 22 July 2026

can be maintained (Dong et al., 2021). Lindzen and Tung (1976) described a ducting framework bounded below by the ground and above by an atmospheric reflector in which the vertical wavelength L and the duct depth H satisfy the resonance condition $\frac{H}{L} = \frac{1}{4} + \frac{n}{2}$, where n denotes the mode number. This relationship indicates that changes in duct depth can modify the set of permitted trapped modes and thereby alter the dominant wave signal sustained within the duct. Because the intrinsic frequency of a gravity wave is linked to the wavevector through the dispersion relation (Fritts & Alexander, 2003), a change in the permitted vertical mode can be accompanied by adjustments in vertical wavenumber, horizontal wavelength, and hence intrinsic period. From this perspective, the observed shortening of the dominant period is consistent with an evolving mode-selection process as the duct was compressed by the strengthening and upward development of the lower-level easterly jet.

It should be emphasized, however, that the frequency observed at a fixed lidar site is not determined by modal selection alone. Ground-based measurements record an apparent frequency that reflects both the intrinsic wave frequency and the Doppler shifting imposed by the background flow; accordingly, changes in the ambient wind can modify the observed period even when the intrinsic wave properties remain unchanged. However, due to the current reliance on single-station observations, a direct quantitative decomposition of these modal transitions remains elusive. A more rigorous attribution analysis would require coordinated multi-point observations or dedicated numerical modal analysis to simultaneously constrain the evolution of horizontal wavelength, phase speed, and intrinsic frequency.

Although the framework outlined above provides a plausible interpretation of the excitation, trapping, and frequency evolution of the observed gravity waves, the wave events remained relatively short-lived. Despite reaching appreciable amplitudes during the active stage, the wave signals decayed rapidly thereafter. One possible explanation is the formation of a critical layer within the westerly jet, where the horizontal phase speed of the waves approached the background wind speed. Under such conditions, wave energy could be efficiently absorbed by the mean flow, thereby weakening or terminating the observable wave activity (Nappo & Chimonas, 1992).

4. Conclusion

Based on CDWL observations, ERA5 reanalysis, and WRF simulations, this study investigated nocturnal tropospheric gravity waves embedded in a double-jet environment over the southern margin of the Taklimakan Desert. The main findings are summarized as follows.

1. Clear nocturnal tropospheric gravity-wave perturbations were observed over the southern margin of the Taklimakan Desert. In all three cases, the waves occurred within a characteristic double-jet environment, consisting of a lower-level easterly jet below 4 km, an upper-level westerly jet at 6-7 km, and a weak-wind layer in between. The observed wave perturbations had dominant periods of 10-20 min, with the largest amplitudes located near the strong vertical wind shear at the base of the westerly jet. Together with enhanced static stability, this shear zone provided favorable conditions for wave generation.

2. The observed wave activity was consistent with the combined effects of thermal and Doppler ducting. The stable layer associated with the temperature inversion acted as a thermal duct, while the jet shear structure contributed to Doppler ducting. Together, these processes limited vertical energy leakage and favored wave trapping within a relatively narrow altitude range.

3. The lower-level easterly jet likely acted as an additional reflecting boundary through the associated evanescent layer, further restricting the vertical space available for wave propagation. Together with

https://doi.org/10.5194/egusphere-2026-2865
Preprint. Discussion started: 22 July 2026

possible critical-level absorption within the westerly jet, this may also help explain the short-lived character of the observed wave events.

4. The observed evolution of dominant wave period appears to be related to changes in duct structure as the easterly jet developed. As the lower-level easterly jet intensified, the ducted layer became vertically compressed and the dominant wave period shifted from longer to shorter values within the observed 10-20 min range. The results are consistent with the interpretation that an evolving waveguide modified the set of permitted trapped modes, thereby contributing to the shift toward higher frequencies. However, the present data do not allow a quantitative separation of modal selection, dispersion effects, and Doppler shifting by the background flow.

Overall, this study provides case-based observational and modeling evidence that the double-jet structure over the southern Taklimakan Desert can act as an effective waveguiding environment for nocturnal tropospheric gravity waves. The high temporal and vertical resolution of the CDWL measurements enabled the detection of fine-scale wave signatures that are not readily resolved by conventional observing systems, while the numerical simulations provided complementary information on horizontal structure, phase speed, and the ducting environment. Taken together, the results suggest that jet-induced duct structures can selectively trap and filter gravity-wave modes and modulate their vertical confinement and frequency evolution in this topographically complex region.

These findings are consistent with previous studies showing that stable layers and background wind shear can support ducted gravity waves. However, most previous observational and modeling studies have emphasized gravity waves in the stratosphere and higher atmosphere, or have focused on more classical sources such as topography, convection, and frontal systems. The present study extends this understanding by showing that a nocturnal lower-tropospheric double-jet structure can itself form an effective waveguiding environment. In this sense, the results provide new observational and modeling evidence that jet-induced ducting can modulate not only the vertical confinement of tropospheric gravity waves but also their frequency evolution.

Several limitations should nevertheless be acknowledged. First, single-station lidar observations cannot directly resolve the horizontal structure of the waves, so estimates of horizontal wavelength, phase speed, and propagation direction depend partly on WRF simulations. Second, the model exhibits a systematic low bias of about 1 km in the simulated wave-core altitude, likely related to uncertainties in boundary-layer parameterization and smoothing of the background flow over complex terrain. This bias limits the precision of the model-observation comparison and introduces uncertainty into the diagnosed Q^2 structure.

These limitations also point to several directions for future work. The nearly two years of continuous high-resolution wind observations already collected at Minfeng provide an important basis for future statistical studies of ducted gravity-wave activity over the southern Taklimakan Desert. In addition, coordinated observations using multiple Doppler lidars would allow direct retrieval of horizontal wave structure and propagation characteristics, substantially reducing the present reliance on numerical simulations. More broadly, the present results suggest that lower-tropospheric ducting in double-jet environments may represent an underrepresented process in gravity-wave parameterization, particularly with respect to wave trapping, spectral filtering, and the selective transmission of wave energy.

Data availability. ERA5 reanalysis data are publicly available from the Copernicus Climate Data Store (CDS; https://cds.climate.copernicus.eu/datasets). DEM data for the Xinjiang region of China are available from the CASEarth Data Sharing Service System (https://data.casearth.cn/thematic/dem/462).

https://doi.org/10.5194/egusphere-2026-2865
Preprint. Discussion started: 22 July 2026

The lidar observations and WRF model simulation outputs used in this study are available from the corresponding author upon reasonable request.

Author contributions. SL and TW conceived and designed the study. TW and FW conducted the lidar observations. FW performed the WRF simulations. SL led the analysis of the lidar and WRF data. XL and SL analyzed the ERA5 reanalysis and radiosonde data. SL prepared the manuscript with contributions from all co-authors. NZ, QH and YW provided theoretical guidance and critical revisions. HX supervised the project, provided research resources, and contributed to the interpretation of the results. All authors reviewed and approved the final manuscript.

Competing interests. The contact author has declared that none of the authors has any competing interests.

Acknowledgements

Financial support

Reference

Alexander, M. J., & Grimsdell, A. W. (2013). Seasonal cycle of orographic gravity wave occurrence above small islands in the southern hemisphere: Implications for effects on the general circulation. *Journal of Geophysical Research: Atmospheres*, *118*(20), 11,589-11,599. https://doi.org/10.1002/2013JD020526

Alexander, M. J., & Holton, J. R. (1997). A Model Study of Zonal Forcing in the Equatorial Stratosphere by Convectively Induced Gravity Waves. *Journal of the Atmospheric Sciences*, *54*(3), 408–419. https://doi.org/10.1175/1520-0469(1997)054%3C0408:AMSOZF%3E2.0.CO;2

Baumgarten, G., Fiedler, J., Hildebrand, J., & Lübken, F.-J. (2015). Inertia gravity wave in the stratosphere and mesosphere observed by doppler wind and temperature lidar. *Geophysical Research Letters*, *42*(24), 1–8. https://doi.org/10.1002/2015GL066991

Bramberger, M., Dörnbrack, A., Bossert, K., Ehard, B., Fritts, D. C., Kaifler, B., Mallaun, C., Orr, A., Pautet, P.-D., Rapp, M., Taylor, M. J., Vosper, S., Williams, B. P., & Witschas, B. (2017). Does strong tropospheric forcing cause large-amplitude mesospheric gravity waves? A DEEPWAVE case study. *Journal of Geophysical Research: Atmospheres*, *122*(21), 11,422-11,443. https://doi.org/10.1002/2017JD027371

Chen, F., & Dudhia, J. (2001). Coupling an Advanced Land Surface–Hydrology Model with the Penn State–NCAR MM5 Modeling System. Part I: Model Implementation and Sensitivity. *Monthly Weather Review*, *129*(4), 569–585. https://doi.org/10.1175/1520-0493(2001)129%3C0569:CAALSH%3E2.0.CO;2

Chimonas, G., & Hines, C. O. (1986). Doppler ducting of atmospheric gravity waves. *Journal of Geophysical Research: Atmospheres*, *91*(D1), 1219–1230. https://doi.org/10.1029/JD091iD01p01219

Chouza, F., Reitebuch, O., Jähn, M., Rahm, S., & Weinzierl, B. (2016). Vertical wind retrieved by airborne lidar and analysis of island induced gravity waves in combination with numerical models and in situ particle measurements. *Atmospheric Chemistry and Physics*, *16*(7), 4675–4692. https://doi.org/10.5194/acp-16-4675-2016

Costantino, L., & Heinrich, P. (2014). *Analysis of gravity wave propagation and properties, comparison between WRF model simulations and LIDAR data in southern France*. 5209. https://ui.adsabs.harvard.edu/abs/2014EGUGA..16.5209C

Costantino, L., Heinrich, P., Mzé, N., & Hauchecorne, A. (2015). Convective gravity wave propagation and breaking in the stratosphere: Comparison between WRF model simulations and lidar data. *Annales Geophysicae*, *33*(9), 1155–1171. https://doi.org/10.5194/angeo-33-1155-2015

https://doi.org/10.5194/egusphere-2026-2865
Preprint. Discussion started: 22 July 2026

Ding, J., Ren, Y., Zhang, H., Chang, H., Hu, Z., Liang, J., Zhang, K., Wang, S., Cao, X., Tian, P., & Zhang, L. (2025). Mechanism of turbulence structure evolution in the nocturnal boundary layer during the interaction of low-level jet and internal gravity waves: Based on full boundary layer turbulence observations. *Journal of Geophysical Research: Atmospheres*, *130*(6), e2024JD042106. https://doi.org/10.1029/2024JD042106

Dong, W., Hickey, M. P., & Zhang, S. (2021). A numerical study of gravity waves propagation characteristics in the mesospheric doppler duct. *Journal of Geophysical Research: Atmospheres*, *126*(13), e2021JD034680. https://doi.org/10.1029/2021JD034680

Dou, X., Han, Y., Sun, D., Xia, H., & Et., A. (2014). Mobile rayleigh doppler lidar for wind and temperature measurements in the stratosphere and lower mesosphere. *Optics Express*. https://doi.org/10.1364/OE.22.0A1203

Durran, D. R. (1990). Mountain waves and downslope winds. In R. M. Banta, G. Berri, W. Blumen, D. J. Carruthers, G. A. Dalu, D. R. Durran, J. Egger, J. R. Garratt, S. R. Hanna, J. C. R. Hunt, R. N. Meroney, W. Miller, W. D. Neff, M. Nicolini, J. Paegle, R. A. Pielke, R. B. Smith, D. G. Strimaitis, T. Vukicevic, & C. D. Whiteman, *Atmospheric processes over complex terrain* (pp. 59–81). American Meteorological Society. https://doi.org/10.1007/978-1-935704-25-6_4

Elshora, M., Su, L., Wei, T., & Xia, H. (2025). Structure, mechanisms, and impacts of nocturnal downslope wind events in the taklimakan desert. *Remote Sensing*, *17*(17), 2984. https://doi.org/10.3390/rs17172984

Elshora, M., Xia, H., Su, L., & Wei, T. (2024). Observation and study of consecutive dust storms in the taklimakan desert from march 16 to 27, 2022, using reanalysis models and lidar. *Atmospheric Research*, *305*, 107431. https://doi.org/10.1016/j.atmosres.2024.107431

Fritts, D. C., & Alexander, M. J. (2003). Gravity wave dynamics and effects in the middle atmosphere. *Reviews of Geophysics*, *41*(1). https://doi.org/10.1029/2001RG000106

Fritts, D. C., & Nastrom, G. D. (1992). Sources of mesoscale variability of gravity waves. Part II: Frontal, convective, and jet stream excitation. *Journal of the Atmospheric Sciences*, *49*(2), 111–127. https://doi.org/10.1175/1520-0469(1992)049%3C0111:SOMVOG%3E2.0.CO;2

Fritts, D. C., & Yuan, L. (1989). An analysis of gravity wave ducting in the atmosphere: Eckart's resonances in thermal and doppler ducts. *Journal of Geophysical Research: Atmospheres*, *94*(D15), 18455–18466. https://doi.org/10.1029/JD094iD15p18455

Ge, J., Huang, J., Weng, F., & Sun, W. (2008). Effects of dust storms on microwave radiation based on satellite observation and model simulation over the Taklamakan desert. *Atmospheric Chemistry and Physics*, *8*(16), 4903–4909. https://doi.org/10.5194/acp-8-4903-2008

Ge, J. M., Liu, H., Huang, J., & Fu, Q. (2016). Taklimakan desert nocturnal low-level jet: Climatology and dust activity. *Atmospheric Chemistry and Physics*, *16*(12), 7773–7783. https://doi.org/10.5194/acp-16-7773-2016

Gill, A. E., & Donn, W. L. (2016). *Atmosphere-ocean dynamics* (1. Aufl). Elsevier Reference Monographs.

Gisinger, S., Wagner, J., & Witschas, B. (2020). Airborne measurements and large-eddy simulations of small-scale gravity waves at the tropopause inversion layer over scandinavia. *Atmospheric Chemistry and Physics*, *20*(16), 10091–10109. https://doi.org/10.5194/acp-20-10091-2020

Gorbunov, M., & Kan, V. (2024). The study of internal gravity waves in the Earth's atmosphere by radio occultations: A review. *Remote Sensing*, *16*(2). https://doi.org/10.3390/rs16020221

Hoffmann, L., & Alexander, M. J. (2010). Occurrence frequency of convective gravity waves during the north American thunderstorm season. *Journal of Geophysical Research: Atmospheres*. https://doi.org/10.1029/2010JD014401

Holton, J. R. (1983). The influence of gravity wave breaking on the general circulation of the middle atmosphere. *Journal of the Atmospheric Sciences*. https://doi.org/10.1175/1520-0469(1983)040%3C2497:TIOGWB%3E2.0.CO;2

Hong, S.-Y., & Lim, J.-O. J. (2006). The WRF Single-Moment 6-Class Microphysics Scheme (WSM6). *Asia-Pacific Journal of Atmospheric Sciences*, *42*, 129–151.

Iacono, M. J., Delamere, J. S., Mlawer, E. J., Shephard, M. W., Clough, S. A., & Collins, W. D. (2008). Radiative forcing by long-lived greenhouse gases: Calculations with the AER radiative transfer models. *Journal of Geophysical Research: Atmospheres*, *113*(D13), 2008JD009944. https://doi.org/10.1029/2008JD009944

https://doi.org/10.5194/egusphere-2026-2865
Preprint. Discussion started: 22 July 2026

Jia, M., Yuan, J., Wang, C., Xia, H., Wu, Y., Zhao, L., Wei, T., Wu, J., Wang, L., Gu, S.-Y., Liu, L., Lu, D., Chen, R., Xue, X., & Dou, X. (2019). Long-lived high-frequency gravity waves in the atmospheric boundary layer: Observations and simulations. *Atmospheric Chemistry and Physics*, *19*(24), 15431–15446. https://doi.org/10.5194/acp-19-15431-2019

Kain, J. S. (2004). The kain–fritsch convective parameterization: An update. *Journal of Applied Meteorology*, *43*(1), 171–181. https://doi.org/10.1175/1520-0450(2004)043%3C0170:TKCPAU%3E2.0.CO;2

Knoop, S., Assink, J. D., Leijnse, H., Tijm, S., De Haij, M. J., Bosveld, F. C., Theeuwes, N., Evers, L. G., Unal, C., & Laffineur, Q. (2026). High-resolution observations of a mesoscale gravity wave event in the nocturnal boundary-layer over the netherlands and belgium. *Journal of Geophysical Research: Atmospheres*, *131*(10), e2025JD046018. https://doi.org/10.1029/2025JD046018

Lindzen, R. S., & Tung, K.-K. (1976). Banded convective activity and ducted gravity waves. *Monthly Weather Review*. https://doi.org/10.1175/1520-0493(1976)104%3C1602:BCAADG%3E2.0.CO;2

Lott, F. (2016). A New Theory for Downslope Windstorms and Trapped Mountain Waves. *Journal of the Atmospheric Sciences*, *73*(9), 3585–3597. https://doi.org/10.1175/JAS-D-15-0342.1

Ma, M., & Qin, L. (2025). Analysis of the ducted gravity waves generated by elevated convection over complex terrain in China. *Atmosphere*, *16*(10), 1118. https://doi.org/10.3390/atmos16101118

Mardia, K. V., & Jupp, P. E. (2000). *Directional statistics*. J. Wiley.

Ming, H., Wei, M., & Wang, M. (2019). Quantitative detection of dust storms with the millimeter wave radar in the taklimakan desert. *Atmosphere*, *10*(9). https://doi.org/10.3390/atmos10090511

Miyoshi, Y., Fujiwara, H., Jin, H., & Shinagawa, H. (2014). A global view of gravity waves in the thermosphere simulated by a general circulation model. *Journal of Geophysical Research: Space Physics*, *119*(7), 5807–5820. https://doi.org/10.1002/2014JA019848

Murphy, D. J., Alexander, S. P., Klekociuk, A. R., Love, P. T., & Vincent, R. A. (2014). Radiosonde observations of gravity waves in the lower stratosphere over Davis, Antarctica. *Journal of Geophysical Research: Atmospheres*, *119*(21). https://doi.org/10.1002/2014jd022448

Nakanishi, M., & Niino, H. (2009). Development of an improved turbulence closure model for the atmospheric boundary layer. *Journal of the Meteorological Society of Japan. Ser. II*, *87*(5), 895–912. https://doi.org/10.2151/jmsj.87.895

Nappo, C. J. (2013). *An introduction to atmospheric gravity waves*. Academic Press.

Nappo, C. J., & Chimonas, G. (1992). *Wave exchange between the ground surface and a boundary-layer critical level*. https://journals.ametsoc.org/view/journals/atsc/49/13/1520-0469_1992_049_1075_webtgs_2_0_co_2.xml

Nyassor, P. K., Wrasse, C. M., Paulino, I., Yiğit, E., Tsali-Brown, V. Y., Buriti, R. A., Figueiredo, C. A. O. B., Giongo, G. A., Egito, F., Adebayo, O. M., Takahashi, H., & Gobbi, D. (2025). Momentum flux characteristics of vertically propagating gravity waves. *Atmospheric Chemistry and Physics*, *25*(7), 4053–4082. https://doi.org/10.5194/acp-25-4053-2025

Olson, J. B. (2021). A Description of the MYNN Surface-Layer Scheme. *NOAA Tech Memo #OAR/GSL-67*, 1–26. https://doi.org/10.25923/F6A8-BC75

Olson, J. B., Kenyon, J. S., Angevine, Wayne. A., Brown, J. M., Pagowski, M., & Sušelj, K. (2019). *A description of the MYNN-EDMF scheme and the coupling to other components in WRF–ARW*. 1–42. https://doi.org/10.25923/N9WM-BE49

Plougonven, R., & Zhang, F. (2014). Internal gravity waves from atmospheric jets and fronts. *Reviews of Geophysics*, *52*(1), 33–76. https://doi.org/10.1002/2012RG000419

Plougonven, R., & Zhang, F. (2016). Gravity waves generated by jets and fronts and their relevance for clear-air turbulence. In R. Sharman & T. Lane (Eds), *Aviation turbulence: Processes, detection, prediction* (pp. 385–406). Springer International Publishing. https://doi.org/10.1007/978-3-319-23630-8_19

Rittner, M., Vermeesch, P., Carter, A., Bird, A., Stevens, T., Garzanti, E., Andò, S., Vezzoli, G., Dutt, R., Xu, Z., & Lu, H. (2016). The provenance of taklamakan desert sand. *Earth and Planetary Science Letters*, *437*, 127–137. https://doi.org/10.1016/j.epsl.2015.12.036

https://doi.org/10.5194/egusphere-2026-2865
Preprint. Discussion started: 22 July 2026

Sato, K., & Hirano, S. (2019). The climatology of the brewer–dobson circulation and the contribution of gravity waves. *Atmospheric Chemistry and Physics*, *19*(7), 4517–4539. https://doi.org/10.5194/acp-19-4517-2019

Shangguan, M., Qiu, J., Yuan, J., Shu, Z., Zhou, L., & Xia, H. (2022). Doppler wind lidar from UV to NIR: A review with case study examples. *Frontiers in Remote Sensing*, *2*. https://doi.org/10.3389/frsen.2021.787111

Shangguan, M., Xia, H., Wang, C., Qiu, J., & Et., A. (2017). Dual-frequency doppler lidar for wind detection with a superconducting nanowire single-photon detector. *Optics Letters*. https://doi.org/10.1364/OL.42.003541

Stober, G., Sommer, S., Schult, C., Latteck, R., & Chau, J. L. (2018). Observation of kelvin–helmholtz instabilities and gravity waves in the summer mesopause above andenes in northern Norway. *Atmospheric Chemistry and Physics*, *18*(9), 6721–6732. https://doi.org/10.5194/acp-18-6721-2018

Su, L., Lu, C., Yuan, J., Wang, X., He, Q., & Xia, H. (2024). Measurement report: The promotion of the low-level jet and thermal effects on the development of the deep convective boundary layer at the southern edge of the taklimakan desert. *Atmospheric Chemistry and Physics*, *24*(18), 10947–10963. https://doi.org/10.5194/acp-24-10947-2024

Sun, J., Nappo, C. J., Mahrt, L., Belušić, D., Grisogono, B., Stauffer, D. R., Pulido, M., Staquet, C., Jiang, Q., Pouquet, A., Yagüe, C., Galperin, B., Smith, R. B., Finnigan, J. J., Mayor, S. D., Svensson, G., Grachev, A. A., & Neff, W. D. (2015). Review of wave-turbulence interactions in the stable atmospheric boundary layer. *Reviews of Geophysics*, *53*(3), 956–993. https://doi.org/10.1002/2015RG000487

Sun, W., & Gao, X. (2022). Geomorphology of sand dunes in the taklamakan desert based on ERA5 reanalysis data. *Journal of Arid Environments*, *207*, 104848. https://doi.org/10.1016/j.jaridenv.2022.104848

Tewari, M., Chen, F., Wang, W., Dudhia, J., LeMone, M. A., Gayno, G., Wegiel, J., & Cuenca, R. H. (2004). *14.2a implementation and verification of the unified noah land surface model in the wrf model*. 1–6.

Toms, B. A., Tomaszewski, J. M., Turner, D. D., & Koch, S. E. (2017). Analysis of a Lower-Tropospheric Gravity Wave Train Using Direct and Remote Sensing Measurement Systems. *Monthly Weather Review*, *145*(7), 2791–2812. https://doi.org/10.1175/MWR-D-16-0216.1

Torrence, C., & Compo, G. P. (1998). A practical guide to wavelet analysis. *Bulletin of the American Meteorological Society*, *79*(1), 61–78. https://doi.org/10.1175/1520-0477(1998)079%3C0061:APGTWA%3E2.0.CO;2

Vincent, R. A., & Joan Alexander, M. (2000). Gravity waves in the tropical lower stratosphere: An observational study of seasonal and interannual variability. *Journal of Geophysical Research: Atmospheres*, *105*(D14), 17971–17982. https://doi.org/10.1029/2000JD900196

Wang, M., Wei, T., Lolli, S., Rocadenbosch, F., Salcedo-Bosch, A., Du, Y., Wang, Y., Wang, C., Zong, L., Gu, Y., Wan, B., Su, L., Wei, F., & Xia, H. (2026). A comparative study of low-level jets in different climate regions in China using multi-site doppler wind lidar observations. *IEEE Transactions on Geoscience and Remote Sensing*. https://doi.org/10.1109/TGRS.2026.3672972

Wei, T., Xia, H., Wu, Y., Yuan, J., Wang, C., & Dou, X. (2020). Inversion probability enhancement of all-fiber CDWL by noise modeling and robust fitting. *Optics Express*, *28*(20), 29662. https://doi.org/10.1364/oe.401054

Wei, T., Xia, H., Yue, B., Wu, Y., & Liu, Q. (2021). Remote sensing of raindrop size distribution using the coherent Doppler lidar. *Optics Express*, *29*(11), 17246. https://doi.org/10.1364/OE.426326

Witschas, B., Rahm, S., Dörnbrack, A., Wagner, J., & Rapp, M. (2017). Airborne wind lidar measurements of vertical and horizontal winds for the investigation of orographically induced gravity waves. *Journal of Atmospheric and Oceanic Technology*, *34*(6), 1371–1386. https://doi.org/10.1175/JTECH-D-17-0021.1

Xing, Y., Chen, Y., Yan, S., Cao, X., Zhou, Y., Zhang, X., Shi, T., Niu, X., Wu, D., Cui, J., Zhou, Y., Wang, X., & Pu, W. (2024). Dust storms from the taklamakan desert significantly darken snow surface on surrounding mountains. *Atmospheric Chemistry and Physics*, *24*(9), 5199–5219. https://doi.org/10.5194/acp-24-5199-2024

Xue, X., Sun, D., Xia, H., & Dou, X. (2020). Inertial gravity waves observed by a doppler wind LiDAR and their possible sources. *Earth and Planetary Physics*, *4*(5), 461–471. https://doi.org/10.26464/epp2020039

https://doi.org/10.5194/egusphere-2026-2865
Preprint. Discussion started: 22 July 2026

Yeh, T.-C. (1950). The circulation of the high troposphere over china in the winter of 1945–46. *Tellus*, *2*(3), 173–183. https://doi.org/10.1111/j.2153-3490.1950.tb00329.x

Zaitseva, D., Kallistratova, M., Lyulyukin, V., Kouznetsov, R., & Kuznetsov, D. (2022). On the influence of internal gravity waves on the intensity of turbulence in the atmospheric boundary layer. *IOP Conference Series: Earth and Environmental Science*, *1040*(1), 12034. https://doi.org/10.1088/1755-1315/1040/1/012034

Zhang, J., Guo, J., Zhang, S., & Shao, J. (2022). Inertia-gravity wave energy and instability drive turbulence: Evidence from a near-global high-resolution radiosonde dataset. *Climate Dynamics*, *58*(11), 2927–2939. https://doi.org/10.1007/s00382-021-06075-2

Zu, R., Xue, X., Qiang, M., Yang, B., Qu, J., & Zhang, K. (2008). Characteristics of near-surface wind regimes in the taklimakan desert, china. *Geomorphology*, *96*(1–2), 39–47. https://doi.org/10.1016/j.geomorph.2007.07.008